Metallic Phase and Temperature Dependence of the $\nu = 0$ Quantum Hall State in Bilayer Graphene

Jing Li,[1,†] Hailong Fu,[1] Zhenxi Yin,[1] Kenji Watanabe,[2] Takashi Taniguchi,[2] and Jun Zhu[1,3,*]
[1]*Department of Physics, The Pennsylvania State University, University Park, Pennsylvania 16802, USA*
[2]*National Institute for Material Science, 1-1 Namiki, Tsukuba 305-0044, Japan*
[3]*Center for 2-Dimensional and Layered Materials, The Pennsylvania State University, University Park, Pennsylvania 16802, USA*

(Received 14 August 2018; published 5 March 2019)

The $\nu = 0$ quantum Hall state of bilayer graphene is a fertile playground to realize many-body ground states with various broken symmetries. Here we report the experimental observations of a previously unreported metallic phase. The metallic phase resides in the phase space between the previously identified layer polarized state at large transverse electric field and the canted antiferromagnetic state at small transverse electric field. We also report temperature dependence studies of the quantum spin Hall state of $\nu = 0$. Complex nonmonotonic behavior reveals concomitant bulk and edge conductions and excitations. These results provide a timely experimental update to understand the rich physics of the $\nu = 0$ state.

DOI: 10.1103/PhysRevLett.122.097701

Bilayer graphene (BLG) in a magnetic field B offers an exciting opportunity to examine the emergence of many-body ground states arising from its multiple internal electronic degrees of freedom. The noninteracting and unbiased $\nu = 0$ possesses eight approximately degenerate Landau levels (LLs) labeled by their spin ($\downarrow$ and $\uparrow$), valley (K and K'), and orbital ($N = 0, 1$) quantum numbers. The interplay between Coulomb interactions controlled by a perpendicular magnetic field $B_\perp$ and layer or valley polarization driven by a transverse external electric field D gives rise to many-body ground states with various broken symmetries [1–23]. Effective short-ranged interactions, for example, are shown to stabilize a canted spin antiferromagnetic (CAF), layer coherent ground state at small D, which transitions to a fully layer polarized (FLP), spin unpolarized state at large D [9,10]. Experiments to date support this scenario, where a conductance peak is commonly associated with the putative CAF/FLP phase boundary [18,20,23–25]. This line boundary further splits into two branches at high perpendicular magnetic field $B_\perp > 12$ T, with the phase region in between thought to be partially polarized in all indices [20,23,26,27].

Even at a moderate $B_\perp$, calculations including more hopping terms and other symmetry-allowed electron-electron interaction terms have uncovered a more nuanced picture [11,17,26]. For example, theory shows that a broken-$\mathrm{U}(1) \times \mathrm{U}(1)$ phase that is canted in both spin and valley could be stabilized in certain parameter regimes in the vicinity of the CAF/FLP phase boundary [26]. Their experimental plausibility remains to be tested.

The ground state of $\nu = 0$ becomes yet richer when the spin polarization is explicitly controlled. Previous studies showed that the CAF state undergoes a second-order phase transition to a spin ferromagnet (FM) upon the application of a large in-plane magnetic field $B_{//}$. The FM state is a bulk insulator but possesses metallic quantum spin Hall (QSH) edge states [18,21]. The QSH edge states are a promising platform to examine the interactions of helical Luttinger liquid [28], and explore the potential realization of an interaction-driven bosonic symmetry protected topological state [29,30]. The pursuit of these intriguing possibilities requires substantial experimental knowledge of the FM (QSH) state, which is currently lacking.

The purpose of this Letter is twofold. We first report the observation of a previously unreported metallic (M) phase of $\nu = 0$. The M phase is marked by very sharp conductance changes and occupies a large phase space in the vicinity of the previously observed CAF/FLP phase boundary. We discuss its possible origins. The M phase persists in a large $B_{//}$, with a temperature dependence that is distinct from the CAF or FM phases. We also conducted a systematic study of the temperature-dependent conductance of the FM phase. The results indicate contributions from both bulk and edge conducting channels and their temperature-dependent excitations. Our results provide fresh input to further understand the fascinating behavior of the $\nu = 0$ state in BLG.

Our measurements employ two-terminal, dual-gated, hexagonal boron nitride (h-BN) encapsulated BLG devices, an exemplary optical micrograph and schematic side view of which are shown in Figs. 1(a) and 1(b). The fabrication of the devices uses van der Waals transfer stacking, side contacts, and a multilayer graphite local bottom gate to screen charged impurities [23,31]. The dual-gated region is connected to the side contacts through regions heavily doped by the Si backgate. The total resistance outside the

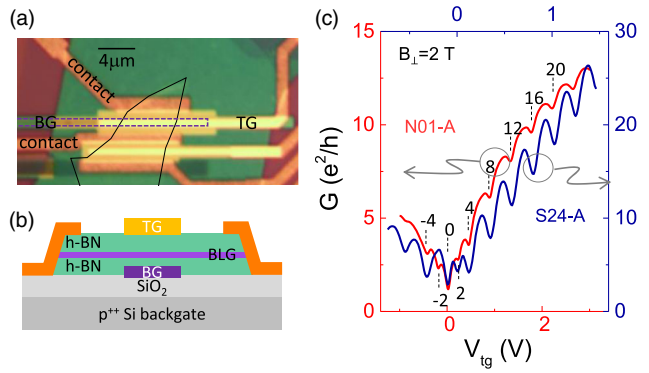

FIG. 1. (a) The optical micrograph of device N01-A. The thin black line outlines the BLG sheet. The local bottom gate (BG) is outlined in dashed purple. The top gate (TG) overlaps the BG over the BLG sheet. The two side contacts are as labeled. (b) A schematic side view of the device. The TG and side contacts are made of Cr/Au and the BG is made of multilayer graphite. (c) Two terminal conductance G (V_{TG}) in devices N01-A (red trace and left and bottom axes) and S24-A (blue trace and top and right axes) at $B_\perp = 2$ T. $V_{\mathrm{BG}} = 0$ V, $V_{\mathrm{Si}} = 40$ V, and $T = 0.3$ K for both traces. The filling factors are marked in the figure.

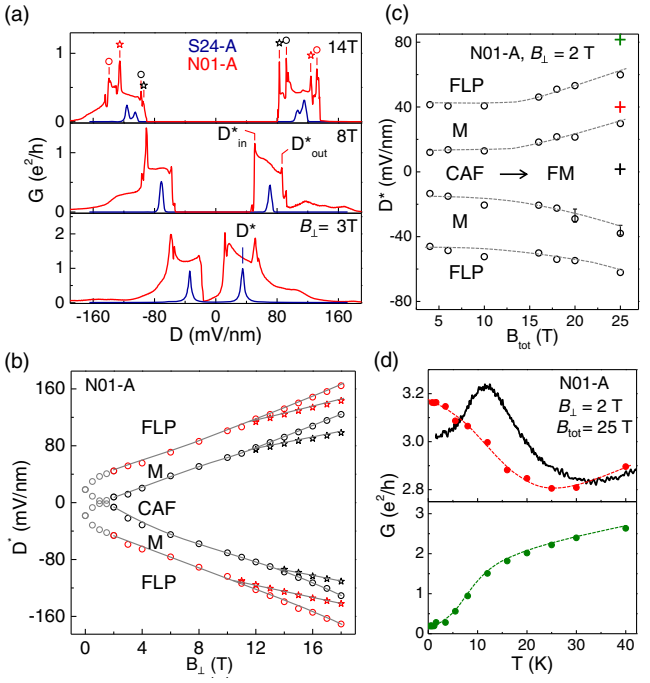

FIG. 2. (a) Comparison of G (D) in device N01-A (red traces) and S24-A (blue traces) at $B_\perp = 3$, 8, and 14 T. Thin vertical lines and symbols mark D^* in S24-A and $D^*_{\mathrm{in/out}}$ in N01-A. $D^*_{\mathrm{in/out}}$ follow a prominent peak consistently as $B_\perp$ evolves. $T = 20$ mK for the red traces and $T = 1.4$ K for the blue traces. (b) (D^*, $B_\perp$) phase diagram of N01-A constructed from data in (a) and additional data given in Figs. S3 and S4 [32]. Below 2 T, boundary conductance peaks (open gray circles) are present although the conductance of the CAF phase does not drop to zero (See Fig. S3 [32]). Gray lines are guide to the eye. (c) The (D^*, B_{tot}) phase diagram of N01-A constructed from data in Fig. S7. Dashed lines are guide to the eye. The three "+" symbols mark the spots where T-dependent conductance $G(T)$ measurements were taken and plotted in (d). $D^* = 0$, 38.2, and 80.1 mV/nm, respectively, for the black, green, and red spots. $B_\perp = 2$ T and $B_{\mathrm{tot}} = 25$ T for all three.

dual-gated region is less than 300 Ω (See Fig. S2 [32]) and not subtracted from measurements. Our devices are in a "wide bar" geometry as Fig. 1(a) shows. They are separated into two groups labeled as "standard" (S) or "new" (N). Figure 1(c) compares the two-terminal conductance of devices N01-A and S01-A at magnetic field $B = 2$ T. Both exhibit strong quantum Hall effect including the appearance of $\nu = \pm 2$ at this low B field, indicating high sample quality. (See Sec. I of the Supplemental Material [32] for the fabrication and characteristics of the devices).

We obtain the displacement field D dependence of the two-terminal conductance G (D) by sweeping the top and bottom gates (TG and BG) simultaneously while maintaining $\nu = 0$ [35,36] (See Sec. I of the Supplemental Material [32] for a description of methods). Figure 2(a) compares G (D) obtained in devices S24-A and N01-A at selected $B_\perp$ fields. S24-A (blue traces) exhibits the standard behavior, where the CAF/FLP phase transition is marked by a single conductance peak labeled as D^* in the plot. In device N01-A (red traces), this peak is widened to a region of high conductance defined by two peaks labeled as D^*_{in} and D^*_{out}. Both D^* and $D^*_{\mathrm{in/out}}$ increase with increasing B, each peak splitting into two at $B_\perp > 11$ T. In the top panel of Fig. 2(a), we mark the four conductance peaks in N01-A using stars and circles. The conductance of regions in between neighboring peaks slowly decreases with increasing $B_\perp$ but remains substantial [See Figs. S3–S4 for additional G (D, B) data in N01-A in the field range of 0–18 T [32]]. The lack of a clear temperature dependence at temperatures below 1 K is consistent with a metallic nature of the state. (See Fig. S5 [32] for data). By tracking the $B_\perp$ evolution of the conductance peaks, we have constructed a new phase diagram for N01-A and plotted it in Fig. 2(b). This phase diagram is reproducible from cooldown to cooldown and is also observed in a second device N01-B (See Fig. S6 [32]). The most remarkable feature of this phase diagram is the prominent appearance of the metallic region. The M phase persists when an in-plane magnetic field component $B_{//}$ is added. In Fig. S7 of the Supplemental Material [32], we show $G(D)$ at a fixed $B_\perp = 2$ T but with increasing total field B_{tot} up to 25 T. Here $B^2_{\mathrm{tot}} = B^2_{//} + B^2_\perp$. The conductance of the M phase increases with increasing B_{tot} and reaches about 3.2 e^2/h at $B_{\mathrm{tot}} = 25$ T. Figure 2(c) plots the phase diagram in the (D^*, B_{tot}) plane constructed from the data in Fig. S7 [32]. The width of the M phases in D appears to be approximately constant on this diagram. Figure 2(d) compares the T-dependent conductance G (T) measured at three locations marked by the "+" symbols. The state inside the M phase

(red trace) exhibits a clear metallic behavior below 25 K. The state inside the FLP phase (green trace) is insulating while the state inside the FM phase (black trace) exhibits a nonmonotonic G (T), which we will discuss later. The behavior of the M phase in a large B_{tot} imposes additional constraints on its potential interpretations.

To understand the origin of the M phase, we examined several scenarios. First of all, device N01-A exhibits a small carrier density broadening of $\delta n \sim 6 \times 10^9$ cm^{-2} (Fig. S2 [32]) and very abrupt transitions of $\delta D \sim 2$ mV/nm in Fig. 2(a). The high sample quality rules out disorder broadening as the source of the wide high-conductance region. Comparing the phase diagrams of the S-type and N-type devices, we see that *superficially* the new phase diagram resembles the "sum" of two standard phases diagrams, offset by $\Delta D \sim 40$ mV/nm from one another. One hypothetic scenario would be that the device consisted of two areas experiencing different D fields and the M region is composed of CAF and FLP states existing in different areas of the sample. This is a highly unusual experimental situation, since a net change in D, without change in n, requires concerted unintentional doping from the top and bottom graphene/h-BN interfaces. Examining the fabrication of both S- and N-type devices carefully we could not see how such a situation could occur in our devices. Nor has it been reported by other groups. Nonetheless we have simulated in Fig. S8 in Ref. [32] the total conductance of a device consisting of two areas experiencing different D fields and show that it could not explain the high conductance of the M phase.

In the standard devices, the conductance peak at the first-order CAF/FLP transition (D^*) in Fig. 2(a) is attributed to a microscopic network of CAF and FLP phases [18,20,23–25]. Applied to the M phase, this network model would imply that the CAF/FLP phase transition occurs over an extended range of the D field, which seems highly unusual for first-order transitions. In the literature, an insulator-metal-insulator phase transition was proposed to explain the experimentally observed nonscaling behavior in the quantum Hall regime [37]. However, that is an unusual case with physics specific to the quantum Hall systems.

Alternatively, the M phase could be a new ground state with a different broken symmetry. Candidates include, for example, a spin-valley entangled phase and a broken-$\mathrm{U}(1) \times \mathrm{U}(1)$ phase as discussed by Murthy *et al.* [26]. The splitting at higher $B_\perp$ can also, in principle, arise from additional predicted phases [26]. These new broken symmetry states produce conductance broadly consistent with our observations and we hope that our results stimulate more studies to directly probe their order parameters. Towards this goal, we note that the h-BN encapsulation layers used in our N devices (56/57 nm, See Table S1 in the Supplemental Material [32]) is much thicker than a typical thickness of 15–30 nm used by us and others. Whether and how this impacts the ground state of $\nu = 0$ require more systematic studies to clarify. It is also worth noting that suspended BLG devices also exhibit both the "standard" (Fig. 2 of Ref. [5]) and "new" (Fig. S6 of Ref. [12]) types of CAF/FLP transitions. Additionally, a hint of the metallic phase was perhaps present in Fig. 2(c) of Ref. [18] though stronger disorder made the situation less clear.

We now turn to the temperature dependence of the FM phase, where experimental studies were spotty [18,21]. Figure 3(a) plots a set of G (D) traces in device S24-A at $B_\perp = 2$ T and selected B_{tot}'s ranging 2–31 T. The saturation of $G(0) = 3.9\ e^2/h$ at $B_{\mathrm{tot}} \geq 18$ T supports the $B_{//}$-driven crossover to a bulk FM with QSH edge states, as reported in Maher *et al.* [18]. Here, conductance peaks marking the FM/FLP transitions [D^* in Fig. 3(a)] are sharp

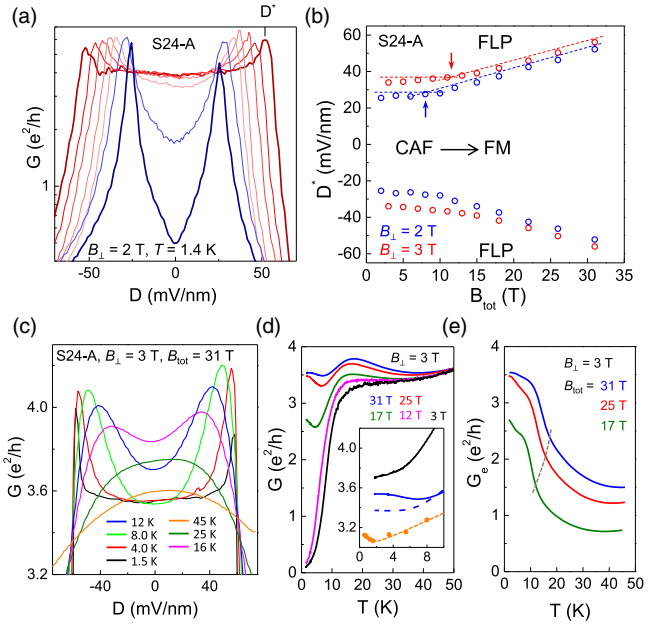

FIG. 3. (a) G (D) of $\nu = 0$ in device S24-A at $B_\perp = 2$ T and selected B_{tot}'s. From blue to red: $B_{\mathrm{tot}} = 2$, 10, 15, 18, 22, 26, and 31 T. (b) (D^*, B_{tot}) phase diagram constructed by reading transition D^*, as marked in (a). $B_\perp = 2(3)$ T for blue (red) symbols. The arrows point to intersections of low-D and high-D trend lines, which are $(B^*_{\mathrm{tot}}, D^*) = (8.3\ \mathrm{T}, 26\ \mathrm{mV/nm})$ and (11.2 T, 34 mV/nm), respectively, for $B_\perp = 2$ and 3 T. (c) G (D) of the same device at selected temperatures as indicated in the plot. $B_\perp = 3$ T and $B_{\mathrm{tot}} = 31$ T. (d) G (T) at $D = 0$. From top to bottom $B_{\mathrm{tot}} = 31$, 25, 17, 12, 3 T. $B_\perp = 3$ T for all traces. Inset: data in the low-T range. The blue solid and dashed traces correspond to $(B_{\mathrm{tot}}, B_\perp) = (31, 3)$ T in two different cooldowns. The black trace corresponds to $(B_{\mathrm{tot}}, B_\perp) = (31, 2)$ T. They are all taken on S24-A. The orange data are from device N01-A at $(B_{\mathrm{tot}}, B_\perp) = (25, 2)$ T. The sign of dG/dT at low temperatures varies among the traces shown. (e) Remaining G_e (T) of top three traces in (d) after subtracting "bulk contribution" as described in the text. The subtracted data are given in Fig. S10 [32]. The dashed line marks the estimated temperatures, below which G_e (T) rises rapidly.

and enable us to determine the phase boundary accurately. Figure 3(b) plots two phase diagrams we obtained at $B_\perp = 2$ and 3 T, respectively, as a function of $B_{\rm tot}$. Following Ref. [18], we identify the crossover field $B^*_{\rm tot}$ as the point where the low and high-D trend lines intersect. $B^*_{\rm tot}$ is, respectively, 8.3 T/11.2 T for $B_\perp = 2$ T/3 T, which is considerably smaller than values reported in Ref. [18], likely due to improved sample quality. We associate the FM/FLP phase boundary with the condition, where the increment of the Zeeman energy $E_z = g\mu_B B_{\rm tot}$ equates the increment of the valley splitting energy Δ_v. Using $\Delta_v = 0.13\,D$ determined previously in Ref. [23] and the slope of $dD^*/dB_{\rm tot} = 1.0$ mV/nm/T in Fig. 3(b), we obtain a g factor of 2.2. This value is in excellent agreement with the expectation of nearly free electrons in graphene.

Next, we investigate the temperature dependence of the CAF and FM states. Figure 3(c) plots an example of G (D) in the FM phase at selected temperatures. As T increases, the sharp conductance peaks at $\pm D^*$ become increasingly broadened and merge at $T^* \sim 25$ K. Meanwhile, the small D region occupied by the FM phase at lower temperatures remains metallic and its transition to the insulating FLP phase at large D is well defined by a "bundle" point. This suggests that the FM phase melts to a metallic state at high temperature [38]. Indeed, in a single-particle LL picture, the $\nu = 0$ state is a half-filled, metallic QH liquid [1]. T^* thus provides a formation energy scale of the FM phase, which was not determined previously. It is a fraction of the single-particle gap to the $N = 2$ LL, which is about 170 K using band parameter determined in Ref. [39]. This melting transition is difficult to identify in conductance change, since both the edge states and the half-filling QH liquid exhibit similar conductance of $\sim 4\ e^2/h$.

G (T) at varying $B_\perp$ and $B_{\rm tot}$ provides a closer look. Figure 3(d) plots the $D = 0$ G (T) in S24-A at $B_\perp = 3$ T and selected $B_{\rm tot}$'s ranging 3–31 T. In the high temperature limit, all five traces merge and exhibit a slightly positive dG/dT, which is consistent with the temperature dependence of a half-filled QH liquid. As T decreases and the CAF or FM state forms, G (T) starts to exhibit diverse behaviors. The two lower traces correspond to the CAF state, where the bulk conduction continues to decrease with decreasing temperature (See Fig. S10 [32] for more data and discussions of the CAF state). In the top three traces ($B_{\rm tot} = 17$–31 T), the QSH edge states are developed and the measured G (T) is high but also nonmonotonic. We have verified that this temperature dependence originates from the dual-gated area and is intrinsic to the $\nu = 0$ state. It is not from the contacts or the access region (See discussions of Fig. S2 [32]). A potential explanation arises, by assuming that the bulk of the FM phase exhibits behavior similar to that of the CAF phase, and that the measured G (T) is a sum of the bulk and edge contributions. In this picture, it is perhaps not difficult to see that dG/dT can change sign in different temperature ranges, in sample-dependent and condition-dependent manners. The several datasets we obtained in both new and standard devices and at different $B_\perp$'s are all consistent with this bulk + edge concurrent conduction scenario. Specifically the temperature dependence of the conductance is quite diverse at the lowest temperatures, as a few examples plotted in the inset of Fig. 3(d) show. The dimensions of the device also play a role in the quantitative behavior of G (T). (See Fig. S9 [32] for more discussions).

Finally, we performed a crude "background subtraction" process to estimate the conduction of the edge states in the FM (QSH) phase. For each targeted FM state, we first identify an effective field $B^{\rm eff}_\perp$, at which the FLP/CAF transition occurs at the same D^* as the FLP/FM transition of the targeted FM (QSH) state, using the (D^*, $B_\perp$) and (D^*, $B_{\rm tot}$) phase diagrams of the device together. We obtained $B^{\rm eff}_\perp = 5.9$, 4.9, and 3.7 T, respectively, for the top three curves in Fig. 3(d), where $B_\perp = 3$ T and $B_{\rm tot} = 31$, 25, and 17 T, respectively. We then approximate the bulk G (T) of the FM state by that of the corresponding CAF state—measurement and discussions are given in Fig. S10 of the Supplemental Material [32]—and substrate it from the measured total conductance in Fig. 3(d). The remaining G_e (T) is attributed to the edge states. Figure 3(e) plots G_e (T) of the top three curves in the main panel of Fig. 3(d). The conductance of the edge states rises rapidly with decreasing temperature below 15–20 K. This behavior has a natural explanation. Because the backscattering of the QSH edge states involves spin flips, one way this process can be mediated is through spin wave excitations of the bulk FM [40]. As temperature decreases, such excitations become increasingly suppressed; hence the edge state conductance increases. In addition, the negative dG/dT is also consistent with the temperature dependence predicted for a repulsive helical Luttinger liquid in certain temperature range [40–42]. The differentiation of these two mechanisms will require more studies. Although both scenarios expect a negative dG/dT at low temperature, our observations are more diverse, as the inset of Fig. 3(d) shows. It is possible that such nonuniversal behavior is due to varying bulk contributions in different samples but we also cannot rule out intrinsic behavior of the edge states manifesting differently under different interaction conditions, e.g., different $B_\perp$'s. The complex conductance behavior our measurements revealed makes it clear that understanding the conduction of the bulk FM state is a necessary part of probing the intrinsic behavior of the QSH edge states. Measurements at lower temperature using nonlocal transport geometries [43,44] or controlled tunneling at a quantum point contact will be essential to further explore the exciting prospects of the edge states in bilayer graphene [28–30].

In summary, our systematic study of the $\nu = 0$ quantum Hall state in BLG has produced new information and insights on this fertile many-body platform. A metallic

phase is found in the vicinity of the previously reported CAF/FLP phase boundary, with potential implications for new broken symmetry ground states. The FM (QSH) state is shown to exhibit complex temperature dependence, likely due to significant concomitant contributions from both bulk and edge conductions. We hope that our results stimulate more future theoretical and experimental studies.

Work at Penn State is supported by the NSF through NSF-DMR-1506212 and NSF-DMR-1708972. Work at NIMS is supported by the Elemental Strategy Initiative conducted by the MEXT, Japan and the CREST (JPMJCR15F3), JST. Part of this work was performed at the NHMFL, which was supported by the NSF through NSF-DMR-1157490, NSF-DMR-0084173, and the State of Florida. We thank Herbert Fertig, Efrat Shimshoni, Ganpathy Murthy, Jainendra Jain, and Chaoxing Liu, Chun Ning Lau and Philip Kim for helpful discussions and Jan Jaroszynski of the NHMFL for experimental assistance.

*Corresponding author.
jzhu@phys.psu.edu
†Present address: National High Magnetic Field Laboratory, Los Alamos, NM 87544, USA.

[1] E. McCann and V. Fal'ko, Landau-Level Degeneracy and Quantum Hall Effect in a Graphite Bilayer, Phys. Rev. Lett. **96**, 086805 (2006).
[2] E. V. Castro, N. M. R. Peres, T. Stauber, and N. A. P. Silva, Low-Density Ferromagnetism in Biased Bilayer Graphene, Phys. Rev. Lett. **100**, 186803 (2008).
[3] B. E. Feldman, J. Martin, and A. Yacoby, Broken-symmetry states and divergent resistance in suspended bilayer graphene, Nat. Phys. **5**, 889 (2009).
[4] R. Nandkishore and L. Levitov, Quantum anomalous Hall state in bilayer graphene, Phys. Rev. B **82**, 115124 (2010).
[5] R. T. Weitz, M. T. Allen, B. E. Feldman, J. Martin, and A. Yacoby, Broken-symmetry states in doubly gated suspended bilayer graphene, Science **330**, 812 (2010).
[6] Y. Zhao, P. Cadden-Zimansky, Z. Jiang, and P. Kim, Symmetry Breaking in the Zero-Energy Landau Level in Bilayer Graphene, Phys. Rev. Lett. **104**, 066801 (2010).
[7] O. Vafek and K. Yang, Many-body instability of Coulomb interacting bilayer graphene: Renormalization group approach, Phys. Rev. B **81**, 041401 (2010).
[8] Y. Lemonik, I. L. Aleiner, C. Toke, and V. I. Fal'ko, Spontaneous symmetry breaking and Lifshitz transition in bilayer graphene, Phys. Rev. B **82**, 201408 (2010).
[9] M. Kharitonov, Antiferromagnetic state in bilayer graphene, Phys. Rev. B **86**, 195435 (2012).
[10] M. Kharitonov, Canted Antiferromagnetic Phase of the $\nu = 0$ Quantum Hall State in Bilayer Graphene, Phys. Rev. Lett. **109**, 046803 (2012).
[11] Y. Lemonik, I. Aleiner, and V. I. Fal'ko, Competing nematic, antiferromagnetic, and spin-flux orders in the ground state of bilayer graphene, Phys. Rev. B **85**, 245451 (2012).
[12] J. Velasco, Jr., L. Jing, W. Bao, Y. Lee, P. Kratz, V. Aji, M. Bockrath, C. N. Lau, C. Varma, R. Stillwell, D. Smirnov, F. Zhang, J. Jung, and A. H. MacDonald, Transport spectroscopy of symmetry-broken insulating states in bilayer graphene, Nat. Nanotechnol. **7**, 156 (2012).
[13] A. Veligura, H. J. van Elferen, N. Tombros, J. C. Maan, U. Zeitler, and B. J. van Wees, Transport gap in suspended bilayer graphene at zero magnetic field, Phys. Rev. B **85**, 155412 (2012).
[14] W. Bao, J. Velasco, F. Zhang, L. Jing, B. Standley, D. Smirnov, M. Bockrath, A. H. MacDonald, and C. N. Lau, Evidence for a spontaneous gapped state in ultraclean bilayer graphene, Proc. Natl. Acad. Sci. U.S.A. **109**, 10802 (2012).
[15] F. Zhang and A. H. MacDonald, Distinguishing Spontaneous Quantum Hall States in Bilayer Graphene, Phys. Rev. Lett. **108**, 186804 (2012).
[16] F. Freitag, J. Trbovic, M. Weiss, and C. Schönenberger, Spontaneously Gapped Ground State in Suspended Bilayer Graphene, Phys. Rev. Lett. **108**, 076602 (2012).
[17] J. Lambert and R. Côté, Quantum Hall ferromagnetic phases in the Landau level $N = 0$ of a graphene bilayer, Phys. Rev. B **87**, 115415 (2013).
[18] P. Maher, C. R. Dean, A. F. Young, T. Taniguchi, K. Watanabe, K. L. Shepard, J. Hone, and P. Kim, Evidence for a spin phase transition at charge neutrality in bilayer graphene, Nat. Phys. **9**, 154 (2013).
[19] A. Young, J. Sanchez-Yamagishi, B. Hunt, S. Choi, K. Watanabe, T. Taniguchi, R. Ashoori, and P. Jarillo-Herrero, Tunable symmetry breaking and helical edge transport in a graphene quantum spin Hall state, Nature (London) **505**, 528 (2014).
[20] K. Lee, B. Fallahazad, J. Xue, D. C. Dillen, K. Kim, T. Taniguchi, K. Watanabe, and E. Tutuc, Chemical potential and quantum Hall ferromagnetism in bilayer graphene, Science **345**, 58 (2014).
[21] S. Pezzini, C. Cobaleda, B. A. Piot, V. Bellani, and E. Diez, Critical point for the canted antiferromagnetic to ferromagnetic phase transition at charge neutrality in bilayer graphene, Phys. Rev. B **90**, 121404 (2014).
[22] Y. H. Wu, T. Shi, and J. K. Jain, Non-Abelian parton fractional quantum hall effect in multilayer graphene, Nano Lett. **17**, 4643 (2017).
[23] J. Li, Y. Tupikov, K. Watanabe, T. Taniguchi, and J. Zhu, Effective Landau Level Diagram of Bilayer Graphene, Phys. Rev. Lett. **120**, 047701 (2018).
[24] T. Jungwirth and A. H. Macdonald, Resistance spikes and domain wall loops in Ising quantum Hall ferromagnets, Phys. Rev. Lett. **87**, 216801 (2001).
[25] K. Dhochak, E. Shimshoni, and E. Berg, Spontaneous layer polarization and conducting domain walls in the quantum Hall regime of bilayer graphene, Phys. Rev. B **91**, 165107 (2015).
[26] G. Murthy, E. Shimshoni, and H. A. Fertig, Spin-valley coherent phases of the $\nu = 0$ quantum Hall state in bilayer graphene, Phys. Rev. B **96**, 245125 (2017).
[27] B. M. Hunt, J. I. A. Li, A. A. Zibrov, L. Wang, T. Taniguchi, K. Watanabe, J. Hone, C. R. Dean, M. Zaletel, R. C. Ashoori, and A. F. Young, Direct measurement of discrete valley and orbital quantum numbers in bilayer graphene, Nat. Commun. **8**, 948 (2017).

[28] J. C. Y. Teo and C. L. Kane, Critical behavior of a point contact in a quantum spin Hall insulator, Phys. Rev. B **79**, 235321 (2009).

[29] Z. Bi, R. Zhang, Y.-Z. You, A. Young, L. Balents, C.-X. Liu, and C. Xu, Bilayer Graphene as a Platform for Bosonic Symmetry-Protected Topological States, Phys. Rev. Lett. **118**, 126801 (2017).

[30] R.-X. Zhang and C.-X. Liu, Fingerprints of a Bosonic Symmetry-Protected Topological State in a Quantum Point Contact, Phys. Rev. Lett. **118**, 216803 (2017).

[31] J. Li, R. X. Zhang, Z. Yin, J. Zhang, K. Watanabe, T. Taniguchi, C. X. Liu, and J. Zhu, A valley valve and electron beam splitter, Science **362**, 1149 (2018).

[32] See Supplemental Material at http://link.aps.org/supplemental/10.1103/PhysRevLett.122.097701 for device characterization, additional data on the M phase and the temperature dependence of the FM and CAF phases, which includes Refs. [33,34].

[33] L. Wang, I. Meric, P. Y. Huang, Q. Gao, Y. Gao, H. Tran, T. Taniguchi, K. Watanabe, L. M. Campos, D. A. Muller, J. Guo, P. Kim, J. Hone, K. L. Shepard, and C. R. Dean, One-dimensional electrical contact to a two-dimensional material, Science **342**, 614 (2013).

[34] Y. Zhang, T.-T. Tang, C. Girit, Z. Hao, M. C. Martin, A. Zettl, M. F. Crommie, Y. R. Shen, and F. Wang, Direct observation of a widely tunable bandgap in bilayer graphene, Nature (London) **459**, 820 (2009).

[35] J. Li, K. Wang, K. J. McFaul, Z. Zern, Y. Ren, K. Watanabe, T. Taniguchi, Z. Qiao, and J. Zhu, Gate-controlled topological conducting channels in bilayer graphene, Nat. Nanotechnol. **11**, 1060 (2016).

[36] J. Li, H. Wen, K. Watanabe, T. Taniguchi, and J. Zhu, Gate-Controlled Transmission of Quantum Hall Edge States in Bilayer Graphene, Phys. Rev. Lett. **120**, 057701 (2018).

[37] G. Xiong, S.-D. Wang, Q. Niu, D.-C. Tian, and X. R. Wang, Metallic Phase in Quantum Hall Systems due to Inter-Landau-Band Mixing, Phys. Rev. Lett. **87**, 216802 (2001).

[38] The CAF state in a purely perpendicular magnetic field also melts at comparable temperatures. See Fig. S10 [32] and discussions.

[39] K. Zou, X. Hong, and J. Zhu, Effective mass of electrons and holes in bilayer graphene: Electron-hole asymmetry and electron-electron interaction, Phys. Rev. B **84**, 085408 (2011).

[40] P. Tikhonov E. Shimshoni H. A. Fertig, and G. Murthy, Emergence of helical edge construction in graphene at the $\nu = 0$ quantum hall state, Phys. Rev. B **93**, 115137 (2016).

[41] M. Kharitonov, S. Juergens, and B. Trauzettel, Interplay of topology and interactions in quantum Hall topological insulators: U(1) symmetry, tunable Luttinger liquid, and interaction-induced phase transitions, Phys. Rev. B **94**, 035146 (2016).

[42] H. A. Fertig and L. Brey, Luttinger Liquid at the Edge of Undoped Graphene in a Strong Magnetic Field, Phys. Rev. Lett. **97**, 116805 (2006).

[43] A. Roth, C. Brune, H. Buhmann, L. W. Molenkamp, J. Maciejko, X. L. Qi, and S. C. Zhang, Nonlocal transport in the quantum spin Hall state, Science **325**, 294 (2009).

[44] L. Du, I. Knez, G. Sullivan, and R.-R. Du, Robust Helical Edge Transport in Gated InAs/GaSb Bilayers, Phys. Rev. Lett. **114**, 096802 (2015).